



Kent Academic Repository

Camard, Julien, Marques, Manuel J., Canedo-Ribeiro, Carla, Silvestri, M., Ellis, Peter J.I., Robinson, Gary K., Chavez-Badiola, Alejandro, Griffin, Darren K., Bradu, Adrian and Podoleanu, Adrian G.H. (2024) *Complex master-slave enhanced optical coherence microscopy*. *Optics Continuum*, 3 (3). pp. 324-337.

Downloaded from

<https://kar.kent.ac.uk/105139/> The University of Kent's Academic Repository KAR

The version of record is available from

<https://doi.org/10.1364/OPTCON.518366>

This document version

Publisher pdf

DOI for this version

Licence for this version

CC BY (Attribution)

Additional information

Versions of research works

Versions of Record

If this version is the version of record, it is the same as the published version available on the publisher's web site. Cite as the published version.

Author Accepted Manuscripts

If this document is identified as the Author Accepted Manuscript it is the version after peer review but before type setting, copy editing or publisher branding. Cite as Surname, Initial. (Year) 'Title of article'. To be published in **Title of Journal**, Volume and issue numbers [peer-reviewed accepted version]. Available at: DOI or URL (Accessed: date).

Enquiries

If you have questions about this document contact ResearchSupport@kent.ac.uk. Please include the URL of the record in KAR. If you believe that your, or a third party's rights have been compromised through this document please see our [Take Down policy](https://www.kent.ac.uk/guides/kar-the-kent-academic-repository#policies) (available from <https://www.kent.ac.uk/guides/kar-the-kent-academic-repository#policies>).



Complex master-slave enhanced optical coherence microscopy

JULIEN CAMARD,^{1,*} MANUEL J. MARQUES,¹ 
CARLA CANEDO-RIBEIRO,² GIUSEPPE SILVESTRI,² PETER ELLIS,²
GARY ROBINSON,² ALEJANDRO CHÁVEZ-BADIOLA,^{2,3}
DARREN GRIFFIN,² ADRIAN BRADU,¹ 
AND ADRIAN PODOLEANU¹ 

¹*Applied Optics Group, School of Physics and Astronomy, Division of Natural Sciences, University of Kent, CT2 7NH, Canterbury, UK*

²*Evolution, Reproduction, and Genome Organisation Group, School of Biosciences, Division of Natural Sciences, University of Kent, CT2 7NJ, Canterbury, UK*

³*Conceivable Life Sciences, 1 Warwick Street, London, W1B 5LR, UK*

*jgac2@kent.ac.uk

Abstract: We present an instrument designed to facilitate localization and high-resolution, optical coherence microscopy (OCM) imaging of small biological samples immersed in a medium several orders of magnitude greater in volume. A modified turret-equipped microscope stand was inserted into the sample arm of a spectral domain optical coherence microscopy (SD-OCM) system. The instrument enabled swift change of imaging objectives through the incorporation of complex master-slave interferometry (CMSI), providing tolerance to dispersion for any objective through the acquisition of a few (≥ 2) calibration spectra. We demonstrate the instrument's ability to localize and image samples by providing examples of its application to optical phantoms and to a porcine oocyte immersed in a biological culture medium.

Published by Optica Publishing Group under the terms of the [Creative Commons Attribution 4.0 License](https://creativecommons.org/licenses/by/4.0/). Further distribution of this work must maintain attribution to the author(s) and the published article's title, journal citation, and DOI.

1. Introduction

1.1. Dispersion in Fourier domain optical coherence microscopy

Frequency domain optical coherence tomography (FD-OCT) is an imaging technology that encodes the depth reflectivity profile of a sample into the modulation density of the optical spectrum at the output of an interferometer illuminated by a broadband optical source. Such a modulated spectrum is referred to as a channeled spectrum (CS). In this paper, we will refer to optical coherence microscopy (OCM) as the microscopic, high-numerical aperture (NA) counterpart of OCT.

Frequency domain OCM strategies are divided into two sub-categories: spectral domain (SD)-OCM, where the source is broadband and the detector is a spectrometer, and swept-source (SS)-OCM, where the source is a tunable laser and the detector is a photodetector. In most cases the detected CS is chirped, i.e. the frequency of its modulation varies with wavenumber.

Chirping stems from: (i) the nonlinear relationship between the optical frequency and the time slots containing the succession of optical frequency-resolved elements and (ii) mismatched dispersion between the two arms of the interferometer, which can be caused by the presence of dispersive media of different nature, for instance, the culture solution in which the biological sample is immersed, or by different lengths of dispersive media, such as unequal amounts of glass across both interferometer arms. The latter is exacerbated when using high-NA microscope

objectives, which contain a large number of optical elements. The change of such objectives leads to a change in the amount of mismatched dispersion as well.

In OCM, the larger the optical path difference (OPD), the larger the number of peaks and troughs in the CS and the lower the contrast of the CS modulation. The maximum OPD where modulation is discernible represents a measure of the instantaneous coherence length in SS-OCM [1] and of the coherence length of the dispersed (diffracted) rays in SD-OCM [2].

Let us consider using a mirror in the sample arm of the interferometer. Due to the CS being chirped, a fast Fourier transform (FFT) of the digitized version of the electrical signal delivered by the photodetector in SS-OCM or spectrometer camera in the SD-OCM leads to a broad peak in the A-scan, i.e. to a suboptimal axial resolution of the OCM system.

In a dispersive medium, the group dispersion (GD) can be defined as the variation of the group index with wavelength [3]:

$$GD = \frac{dn_g}{d\lambda} \quad (1)$$

The enlargement of the axial resolution interval due to a dispersive medium can be expressed as a function of GD [3,4]:

$$\delta_{z,eff} = \sqrt{\delta_z^2 + (GDL_g\Delta\lambda)^2} \quad (2)$$

where δ_z is the full width at half maximum (FWHM) roundtrip axial resolution interval for a Gaussian spectrum from a single reflecting surface without dispersion, L_g is the length of the dispersive medium and $\Delta\lambda$ the FWHM source bandwidth.

In a dispersive medium, the axial resolution is degraded according to Eq. (2). As such, high-resolution applications are more demanding in terms of dispersion compensation [5].

To mitigate the effect of non-linear sampling in wavenumber k and the effect of dispersion, the CS data must be processed to be reassembled within linear k slots, resorting to hardware or software-based strategies. To correct for collection of data along time slots that do not align with optical frequency slots, a hardware solution uses a k -linear spectrometer consisting in adding a carefully aligned prism behind a diffraction grating [6]. To compensate for dispersion in the interferometer, hardware solutions employ dispersion compensating glass (DCG) in one or both arms of the interferometer [4,7] or fiber Bragg gratings [8,9].

Compensation of the length of different materials targets at least the 2nd order dispersion (group velocity), that exercises the most significant impact on the interferometric signal [10]. The larger the bandwidth of the optical source in SD-OCM or tuning bandwidth in SS-OCM, the larger the deleterious effect of dispersion left uncompensated. If higher orders of dispersion have to be compensated for, choosing materials of exact length to perfectly compensate the dispersion unbalance is extremely difficult. Grating-based phase delay scanners [11] and dual optical fiber stretchers [12] were also reported for 2nd order dispersion compensation.

Software strategies include data resampling via interpolation methods [13], improved (fractional) Fourier transformations [14] and an iterative method based on phase correction [15]. Recently, techniques based on the acquisition of A-scan spectrograms at each depth [16] and artificial neural networks [17,18] have also been reported.

Master Slave interferometry [19] is an alternative processing technique of the CS producing dispersion tolerant A-scans [20]. Further improvements of the master slave interferometry led to complex master slave interferometry (CMSI), producing complex-valued reflectivities [21] similar to those delivered by conventional FFT-based OCT.

In its implementation, CMSI uses the same interferometer twice: at a master stage, to collect several CS_{exp} (at least two), using a mirror as sample, and at the slave stage, for the effective acquisition, when the sample under study replaces the mirror.

During the calibration process (master stage), at least two CS_{exp} are acquired. These are then used to infer the two following effects:

- the non-linear distribution of wavenumber $\tilde{\nu}$ over time, which is represented by a function $g(\tilde{\nu})$
- the unbalanced dispersion of the interferometer, represented by a function $h(\tilde{\nu})$

The variable $\tilde{\nu}$ is acquired over time in SS-OCM or along the spectrometer linear array cells in SD-OCM.

Using the functions $g(\tilde{\nu})$ and $h(\tilde{\nu})$, complex mask functions are generated for each depth of interest. The masks are top hat-shaped channelled spectra versus wavenumber that are chirped due to the combined effect of nonlinear reading of the spectrum and to the dispersion in the interferometer.

1.2. Different microscope objectives, different fields of view

In conventional microscopy the NA of the optical elements determine the lateral and axial resolutions. Lateral resolution can be defined by the smallest spot to which a lens can focus a beam, which in conventional microscopy is given by the lateral extent of the Airy disc, proportional to λ and inversely proportional to NA. OCM imaging of small organisms thus requires λ to be small (typically around 800 nm if using near-infrared sources) and NA to be high (typically ≥ 0.5). An increase of NA leads to a smaller field of view, which makes the localization of small samples immersed in a medium (and their subsequent high-resolution, large-NA imaging) time consuming and hardly repeatable. For faster examination of a large number of samples with OCM, there is a need for a versatile system enabling quick and reliable changes of imaging lens, which can provide a range of FOV and resolutions adapted to sample localization as well as to sample imaging.

1.3. Dispersion and CMSI

Unlike in confocal microscopy, an increment in magnification in OCM requires additional adjustments in the system. Microscope objectives, depending on the corrections applied (e.g. chromaticity, flat field correction), can be composed of a various number of glass elements [22]. Consequently, a change of microscope objective results in a variation of the amount of glass along the optical axis. This affects the overall OPD and the amount of dispersion in the sample arm. Therefore, each microscope objective modifies the optical path in the sample arm by a different length. This must be compensated by a matched adjustment of the reference arm length.

Adjusting the optical path is common practice in OCM and requires a simple displacement of the reflector in the reference arm. However, dispersion correction requires knowledge of the type of glass and the length of each of the glass element that constitute the microscope objective in order to insert similar glass in the reference arm.

In confocal microscopy, the axial resolution is related to the pinhole size and the optical sources employed usually exhibit a high degree of monochromaticity [23], therefore chromatic dispersion effects are not a problem. Even so, the use of several lasers to excite fluorophores in several wavelength bands has motivated the development of achromatic microscope objectives that can handle large optical bandwidths.

OCM can take advantage of these broadband microscope objectives. To focus the rays irrespective of wavelength demands greater complexity in the structure of objectives. Although variable dispersion inside the objective is corrected, i.e. the dispersion curve across λ is flattened, the total dispersion of the objective, and consequently of an OCM sample arm, increases with the number of optical elements.

Finally, unlike confocal microscopy, OCM relies on interferometry. This is achieved by adjusting the paths traveled by the sample and reference waves within certain limits determined by the axial range of the system. Differences between dispersion encountered by the two waves degrade the quality of the interference pattern. In short, dispersion due to the glass elements in

the microscope objective does not represent a problem for confocal microscopy, but it does for OCM.

In this paper, to address the problem of dispersion variation when changing the microscope objective, we propose to perform CMSI calibration for each of them. At the Master stage, the functions $g(\tilde{\nu})$ and $h(\tilde{\nu})$ are evaluated and are then employed to compute specific masks for each magnification setting, as described in section 1.1 above. In this way, tolerance to dispersion and non-linearity in wavenumber is achieved.

The procedure is applied to a purposely-assembled OCM system employing a repurposed turret-equipped commercial microscope placed in the sample arm between the scanning unit and sample. The assembly, implementing CMSI processing, enables quicker sample localization and centering using initially a low-NA objective, followed by subsequent switches to higher-NA objectives for OCM imaging at higher transversal resolutions.

A turret has previously been used in a system combining optical coherence tomography and confocal microscopy, where the change between both modalities was accompanied by a change in the NA of the interface optics used [24]. Transition between optical coherence tomography and its angiography version was also facilitated by a turret in [25]. However, the problems raised by changing the NA in the part of the system performing OCM were not detailed in either [24] or [25].

2. Spectral domain OCM with simplified magnification change

2.1. Set-up description

A sketch of the SD-OCM system is shown in Fig. 1. A supercontinuum source (SuperK EXR9, NKT Photonics) is coupled to a filtering box (SpectraK Split, NKT Photonics), providing an emission bandwidth centered at 831 nm with a FWHM bandwidth of 141 nm, giving a theoretical axial resolution of 2.16 μm in air.

The sample arm is composed of a repurposed turret-equipped commercial widefield microscope (Laborlux D, Leitz). The microscope turret, T, is equipped with RMS-threaded objectives. The microscope platform offers a fully controllable x,y,z translation stage and takes conventional microscope slides.

The optical beam is scanned along the two lateral directions over the sample by a pair of galvoscanners (G1432, Galvoline) (XGS and YGS), via the selected microscope objective (MO). OCM interference spectra are detected and buffered by a commercial spectrometer, S (Cobra S-800, Wasatch Photonics) and transferred via camera link bus to a frame grabber (PCI-e 1437, National Instruments). An in-house LabVIEW software implements the CMSI processing described above, as well as the display and saving of B-scans.

2.2. Microscope objective description

The operation of the system was proven in imaging using four off-the-shelf microscope objectives. Table 1 details the characteristics of the four objectives, brand, type, magnification, NA and Rayleigh range z_R . Figure 2 shows a picture of the four objectives in (a) as well as their corresponding experimentally-measured confocal gate in (b). The latter was obtained by blocking the reference arm and measuring the power at the interferometer output for various positions of a mirror used as a sample. MO1, MO2 and MO3 were employed for the analysis presented in sections 2.3 and 3.1 to 3.4. MO4 was employed in section 3.4 only.

2.3. Field of view

To assess the capability of our custom SD-OCM system in performing imaging with different magnifications while keeping the feature of interest within the same scanned area, an USAF resolution target was imaged. Triangular and sawtooth signals with amplitude of 0.125 V were

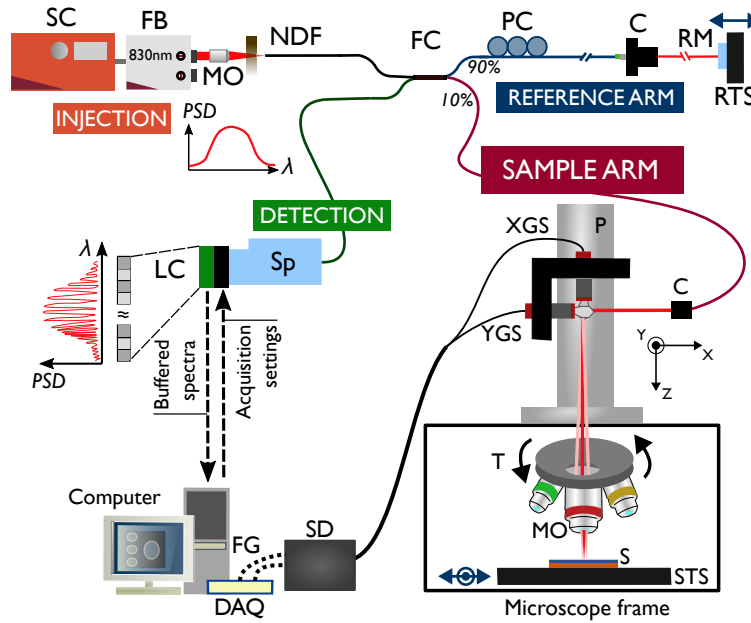


Fig. 1. Diagram of the SD-OCM set-up. SC: Supercontinuum source, FB: Filtering box, MO: Microscope objective, NDF: Neutral density filter, FC: Fiber coupler, PC: Polarization controller, C: Fiber collimator, RM: Reference mirror, RTS: Reference translation stage, P: 1.5” post, XGS/YGS: X and Y galvoscaners, T: Turret, S: Sample, STS: Sample translation stage, Sp: Spectrometer, LC: Line camera, FG: Frame grabber, DAQ: Digital acquisition board, SD: Scanner driver, PSD: Power Spectral Density.

Table 1. Characteristics of MO1, MO2, MO3 and MO4

Microscope obj.	Magnification	NA	Brand	Type	Rayleigh range z_R
MO1	5X	0.16	Zeiss	Plan Neofluar	117 μm
MO2	10X	0.25	Comar	Plan	32.5 μm
MO3	20X	0.50	GS	Phase Contrast	12.3 μm
MO4	20X	0.50	Nikon	Plan Fluor	15.5 μm

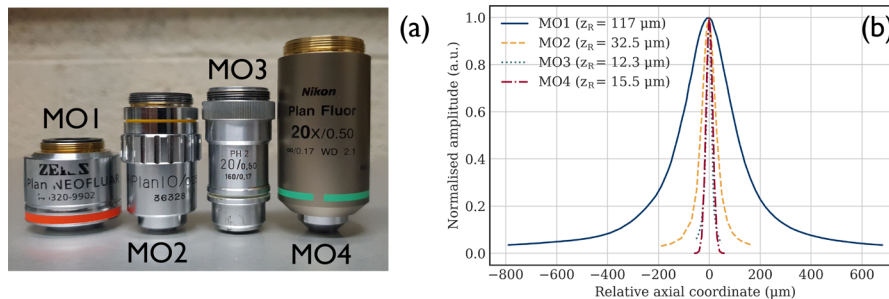


Fig. 2. (a) Photograph of the four microscope objectives employed (MO1, MO2, MO3 and MO4). (b) Plot showing the axial intensity profile of the four microscope objectives employed.

applied to the XGS and YGS galvoscaners, respectively. The resulting square scanned areas were measured to be $650 \pm 20 \mu\text{m}$, $285 \pm 10 \mu\text{m}$ and $171 \pm 5 \mu\text{m}$ using MO1, MO2 and MO3, respectively. Figure 3 shows a single *en face* slice for each objective, as displayed on the front panel of the in-house LabVIEW acquisition program. This program allows for scrolling through depth by changing the mask employed by the CMSI protocol.

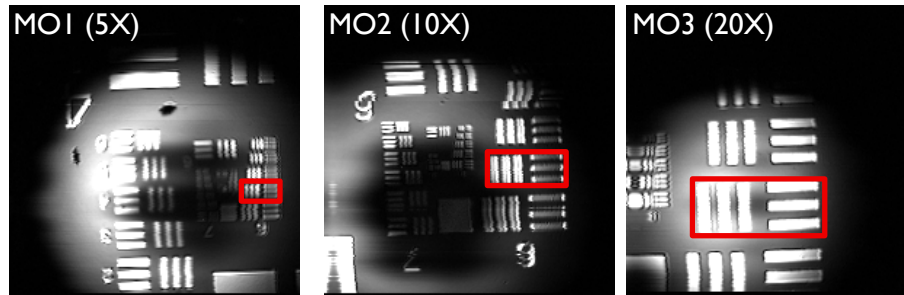


Fig. 3. From left to right, OCM *en face* slices of a USAF target obtained with MO1, MO2 and MO3. The element 3 of group 6 is circled in red. Image sizes are $650 \pm 20 \mu\text{m}$, $285 \pm 10 \mu\text{m}$ and $171 \pm 5 \mu\text{m}$ for MO1, MO2 and MO3, respectively.

The element 3 of group 6, circled in red, stays within the field of view for all microscope objectives used. Some lateral shift from one objective to the next is noticeable; however, the feature of interest is still within the view and the lateral shift can be corrected by actuating on the sample holder stage. The misalignment is mainly due to the turret fabrication, each time the turret is rotated, the new position is dictated by the mechanical assembly of the turret which does not allow for any intermediate position to be manually chosen. We used an off-the-shelf microscope stand with a turret, so we inherited the errors in the fixtures of its elements. We minimized these errors by adjusting the relative position of the scanned beam through the centers of the MOs.

The images for MO1 (5X) and MO2 (10X) show a ring shape (doughnut) while that for MO3 (20X) looks more of a disk. This effect is due to the intersection of the coherence gate with the plane of the USAF target, where the coherence gate is curved due to the fact that the distance from the objective to the scanners is larger than the objective focal length. The coherence gate can be brought to a planar shape by using a telescope, however this would lead to additional optical interfaces and aberrations. Another option is to change the depth of the mask used in agreement with X,Y scanning [26].

While these are valid strategies, it should be highlighted that for small magnification, the ring shape pattern described above is only visible when imaging single-layer, specular planar objects such as mirrors, coins or a USAF target (Fig. 3). When imaging scattering structures with sufficient axial extent, the *en face* view is entirely filled by the portion of the sample volume that is selected by the curved coherence gate. Notably, for larger magnification the displayed lateral size is smaller and the coherence gate becomes closer to a planar surface. The ring shape is thus less visible as shown by the image for 20X.

2.4. Biological sample preparation

Animal handling was performed in accordance with The Animals (Scientific Procedures) Act 1986. Procedures involving live animals were performed at Charles River (Margate, UK) under the scientific supplier's licenses. Schedule 1 culling was performed by trained personnel at the same site.

A CD1 female mouse of 4 weeks of age was subjected to ovarian stimulation following established supplier protocols. Briefly, this involved the intra-peritoneal administration of 7.5 IU pregnant mare serum gonadotrophin (PMSG), followed by 7.5 IU human chorionic gonadotropin

(hCG) after 48h. Culling by cervical dislocation was completed 17h after the second injection. The ampulla was then isolated under a dissecting microscope, and the ovulated oocyte cluster was released in HEPES buffered M2 medium (M7167, Sigma-Aldrich, Gillingham, UK) supplemented with 1 mg/mL hyaluronidase (H3506, Sigma-Aldrich) at 37°C. Oocyte denudation was achieved within 2 min, at which point the oocytes were moved to fresh M2 medium and maintained at 37°C until use. In preparation for OCM observation, the oocytes were rinsed in phosphate-buffered saline (PBS), and placed on a positively charged glass slide (to increase adhesion and reduce the chance of shuffling) in a 10 μL droplet.

3. Results

3.1. Dispersion assessment with CMSI

CMSI masks were generated following the method described in [21]. At the master stage, for each MO, 3 CS_{exp} were acquired for steps in depth z of 0.5 mm, using the RTS in Fig. 1. Then complex masks were calculated. We call GH1, GH2 and GH3 the set of masks computed with MO1, MO2 and MO3, respectively.

The function $h(\tilde{\nu})$, expressing the phase change detected in the CS along the spectrometer pixel array, is represented in Fig. 4 (a) for all three MO. The three traces do not overlap, and there is no apparent relationship between the magnification provided by each objective and their dispersion curve, which highlights the need for objective-specific dispersion correction. The inflexion point where all three traces intersect results from the choice of the integration constant in the derivations presented in [21].

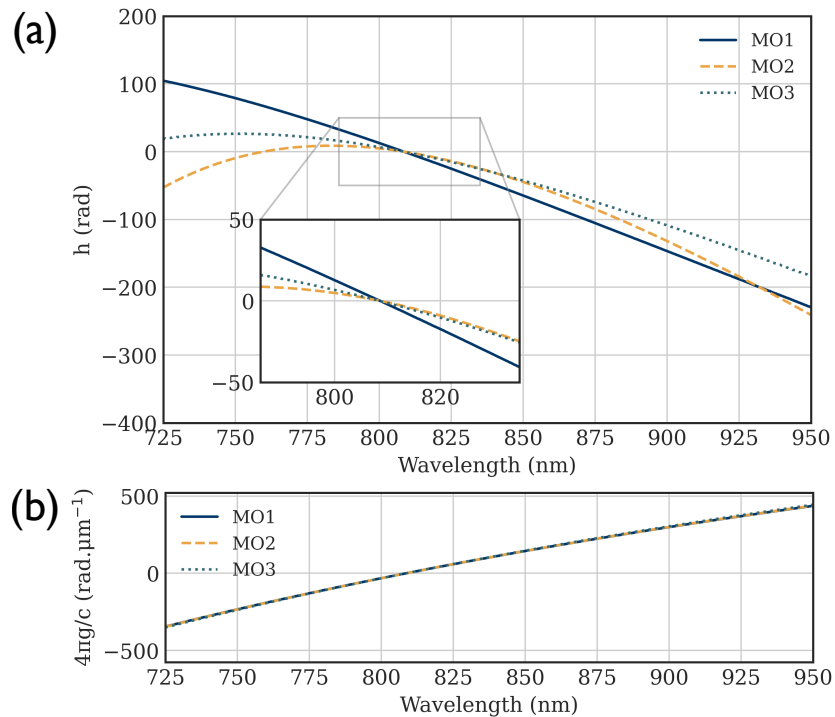


Fig. 4. Plots of functions h (a) and $\frac{4\pi g}{c}$ (b) versus wavelength for the 3 microscope objectives studied (MO1, MO2 and MO3).

The function $\frac{4\pi g(\tilde{\nu})}{c}$ displayed in Fig. 4 (b) shows the non-linear frequency distribution along the spectrometer line camera, LC. The traces for all three objectives are overlapped, showing that $g(\tilde{\nu})$ is not dependent on dispersion effects in the interferometer, as expected. The spectral coordinate chosen to represent this graph is wavelength which was calculated from the pixel divisions of the linear array using manufacturer data.

3.2. A-scan comparison

The importance of matching the right set of masks with a given objective was evaluated by looking at A-scans obtained with a mirror as the sample, with the turret set on MO1.

Figure 5(a) and (b) show a CS as detected by the spectrometer's line array and its corresponding A-scan obtained by FFT, respectively. Due to the chirp in the spectrum versus the time coordinate (not shown), the mirror is represented by a broad A-scan peak with a FWHM of 129 μm .

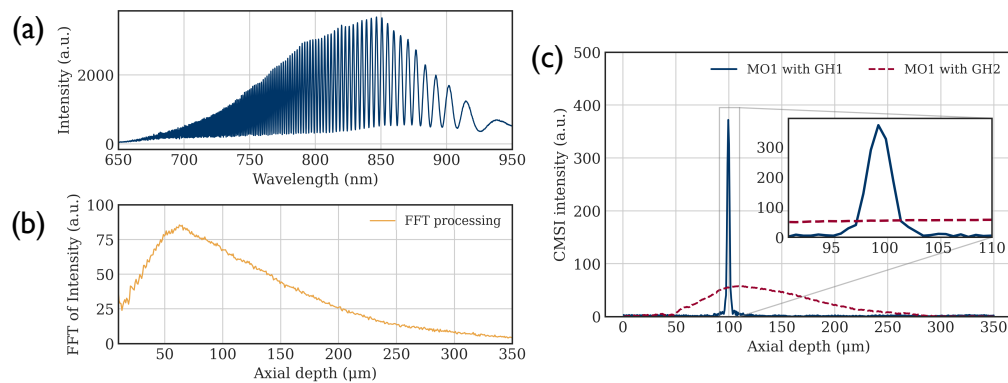


Fig. 5. (a) Channeled spectrum (CS) as detected by the spectrometer line camera, obtained with system described in Fig. 1 using MO1 and a silver mirror as the sample and (b) its Fast Fourier Transform (FFT). (c) Processing of (a) using CMSI employing two sets of masks (GH1 and GH2).

Figure 5 (c) shows the results of processing the same CS with CMSI using two sets of masks: GH1 (calibrated with MO1) and GH2 (calibrated with MO2). When the GH2 set is used, the peak appears broad (yellow), with a FWHM of 112 μm . When the GH1 set is used, a sharp peak is obtained in the A-scan (blue), with a FWHM of 2.60 μm .

Similar deterioration of A-scans was observed by performing the same study with MO2 and MO3, and narrow A-scan peaks were only obtained when using the mask sets GH2 and GH3, respectively (not shown).

The large difference in axial resolution shows how important is to determine the correct set of masks for each objective. The apparent similarity of graphs for g and h in Fig. 4 does not predict the drastic different behaviour demonstrated in Fig. 5 (c).

3.3. B-scan comparison

A phantom made of a layer of lens tissue, three layers of tape and a layer of paper (top to bottom, diagrammatically represented in Fig. 6(a)) was imaged with the SD-OCM system. B-scan images were obtained with the turret selecting either MO1 or MO2. The goal of this experiment was to mimic a protocol where a feature of interest would be localized and imaged initially with a low-NA objective, then imaged with an objective with higher NA. The sample was first imaged with MO1 and the corresponding set of masks, GH1. A B-scan of the phantom obtained with these settings is shown in Fig. 6 (b), where the different phantom layers can be identified. Then, the turret was switched to MO2. A B-scan obtained with MO2 using the same set of masks GH1

is presented in Fig. 6(c) and shows noticeably broadened layers, which makes their identification difficult. Finally, the set of masks GH2 was selected. The B-scan on Fig. 6(d) was obtained with MO2 and GH2. The various layers of the phantom are again well-defined and identifiable.

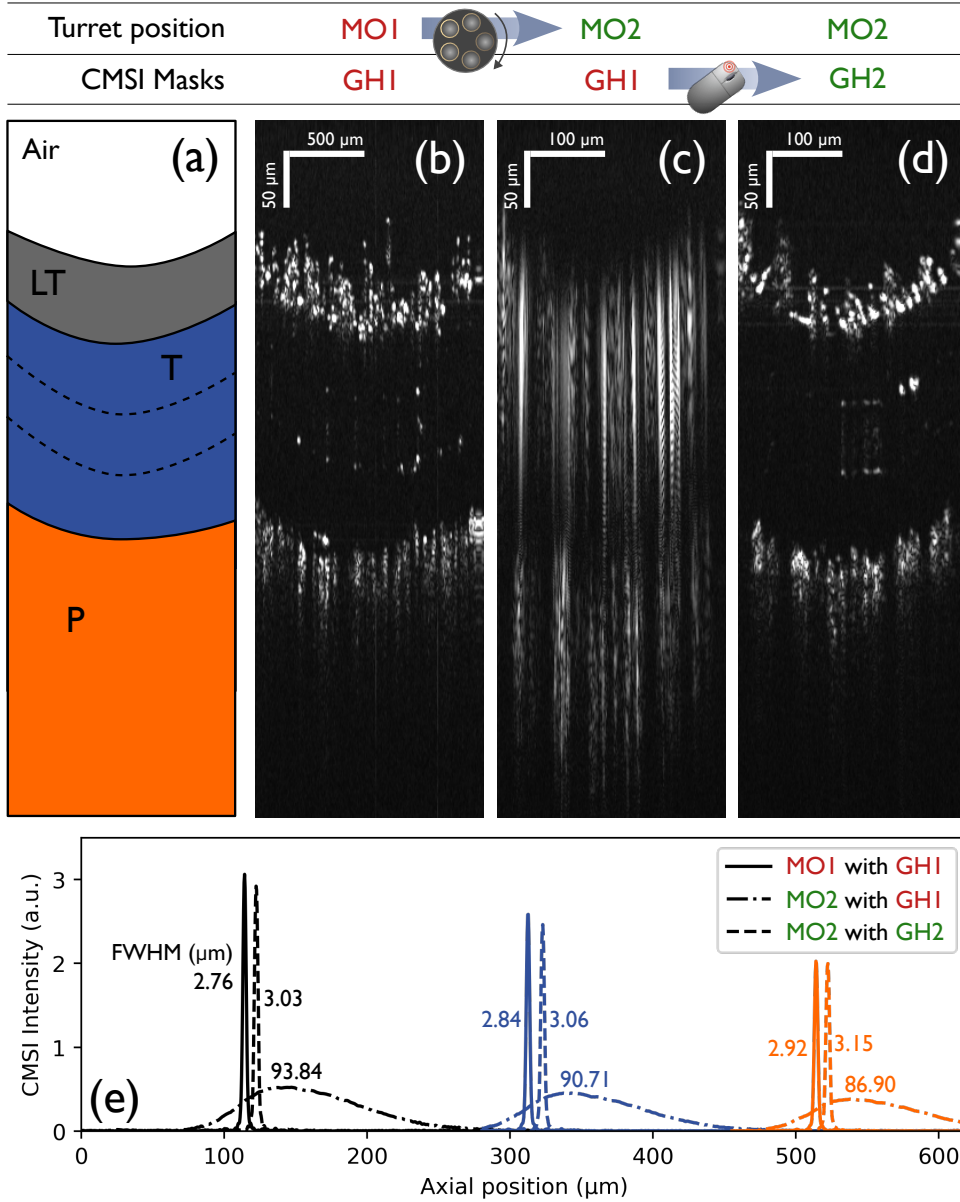


Fig. 6. (a) Layout of a home-made phantom. LT: Lens Tissue. T: Double-sided tape. P: Paper. (b) to (d): B-scan images of the phantom. (b) using MO1 and mask set GH1 (c) using MO2 and mask set GH1 (d) using MO2 and mask set GH2. (e): Line intensity profiles measured at several depths, for each of the pairings in (b-d). The full width at half maximum (FWHM) of each profile is indicated in microns.

For each pairing of turret position with CMSI masks presented in Fig. 6, line intensity profiles were obtained using a mirror as a sample: in Fig. 6 (e) at 3 axial positions. These profiles were

computed by multiplying the masks used in each case (GH1 or GH2) with the CS_{exp} obtained at each of the axial positions. Their positions are located at shallow, medium and deeper depths, with slight variations between pairings. The FWHM value of each profile is indicated in microns next to the corresponding peak. When the mask set GH1 is used with MO1 and when the mask set GH2 is used with MO2, the shallow experimental resolution is close to that reported in Fig. 5.

The slight degradation of the axial resolution with depth over the displayed B-scan axial extent (600 μm) can be explained by increased contribution of multiple scattering. When MO2 is used with GH1, the calculated axial resolution is around 90 μm , which is comparable to the value found for the association of MO1 and GH2, reported in Fig. 5.

3.4. Localization and OCM imaging of a mouse oocyte

The ability of the SD-OCM setup to characterize small biological samples in a medium was assessed by imaging a mouse oocyte immersed in a droplet of PBS on a microscope slide. Because the diameter of the oocyte ($100 \pm 20 \mu\text{m}$) is much smaller than the diameter of the droplet of PBS ($5 \pm 1 \text{ mm}$), it is difficult to locate and identify the oocyte, which is a typical example of the problem faced by users and addressed by this paper.

We first used the lowest-NA objective, MO1 (5X), to scan a large portion of the droplet area. The oocyte was located in the X,Y plane and placed in the center of the field of view using the sample translation stage, STS. Figure 7 (a) shows a frame of the depth-averaged live display used to localize and center the oocyte, obtained with MO1.

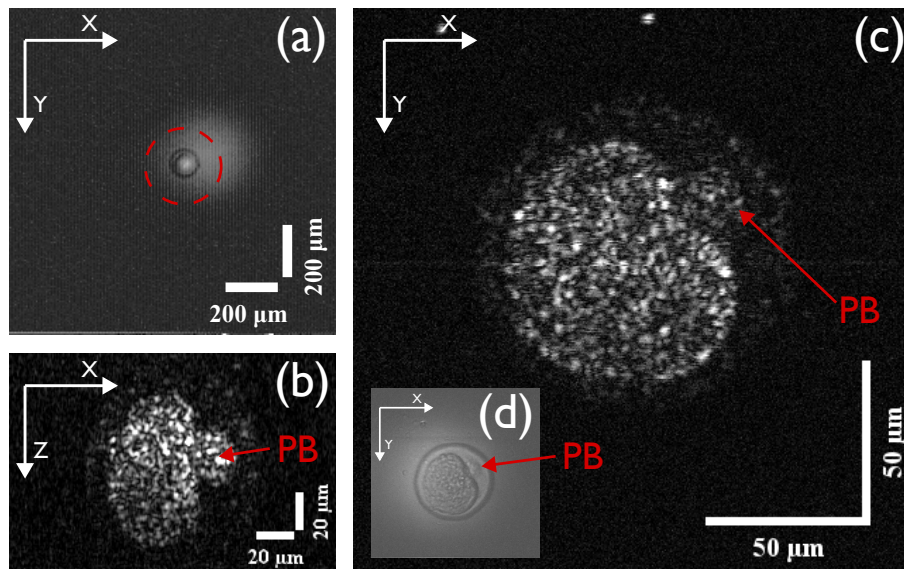


Fig. 7. (a): Depth-averaged image of a mouse oocyte (visible in the dotted circle) immersed into PBS obtained with MO1. (b) to (d): visualizations of the same oocyte obtained with MO4. (b) B-scan image, depth along the vertical, the horizontal size is the same as that of image in (c); (c) *en face* image (d) depth-averaged image. The polar body (PB) is indicated by arrows in (b) to (d).

The turret was rotated to M04 (20X). Centering of the oocyte was adjusted with the STS. A previously computed set of masks for MO4 (GH4) was loaded and three-dimensional OCM data was acquired. Figure 7 (b) to (d) show a B-scan, *en face* image and depth-averaged image of the oocyte, all obtained with MO4. The polar body (PB) is a small cell resulting from oocyte maturation containing discarded genetic material [27]. This cell is particularly significant for in

vitro fertilization (IVF) clinicians, as its presence serves as an indicator of the oocyte's readiness for fertilization. It can be identified on the OCM images and is indicated by the red arrows in Fig. 7 (b) to (d).

It is worth noting that the confocal gate position changes with the objective, hence an intersection of the confocal gates of all MO does not exist. Therefore, axial adjustment of the sample position is necessary after a change of MO. Each time the MO is changed, the first correction is to change the set of masks, followed by bringing the sample in focus by actuating on the vertical position of the STS and maximising the brightness in the depth-averaged image in Fig. 7 (a). This is then followed by moving the RTS to a value already tabulated to match the new optical path difference resulting from the MO change and from the axial shift of the STS. Finally, the coherence gate is finely adjusted by watching the position of the B-scan on the display.

4. Discussion and conclusions

This study was performed with an adapted commercial microscope, however such a turret + translation stage arrangement can be applied to any research OCM system without the need for a microscope stand, e.g. by mounting the turret in a cage system attached to the scanning unit.

The prototype presented here features some imperfections. The slight lateral drift of the region of interest accompanying the objective change demands an extra lateral adjustment of the STS. This can be corrected by adding degrees of translation in the system. Most commercial turrets include adjustment screws to individually adjust the lateral alignment of each objective.

Improvements of the proposed system could also include a motorized sample stage coupled with software-assisted storing of sample coordinates. By knowing the field of view dimensions of a given objective, the feature of interest situated at coordinates $[x, y]$ in the X,Y plane could be translated by $[-x, -y]$. In this way, the feature imaged would remain in the center of the field of view through the process of turret rotation to engage different objectives.

Motorization could also be implemented in the reference arm, as the position of the reference mirror, RM, is unique to each objective, i.e. only as many positions as the number of objectives employed need to be stored. In our practice, we found that using a low-NA objective in confocal mode, i.e. without engaging the reference arm of the OCM system and only looking at the depth-averaged image, was an efficient way to localize and center the oocyte while keeping the reference mirror to the set position for the high-NA OCM imaging.

Common practice in commercial OCM systems requires the replacement of both the scan lens and a dispersion compensation set in the reference arm, which is time-consuming. The method of turret-mounted objectives and CMSI as presented offers a faster way to change the sample lens. The use of a turret not only provides fluid change of magnification but simplifies the utilization of a full set of objectives from the same supplier/series, made to be used together in a conventional microscope. Such a set shares the same mounting thread and employs similar AR coating.

The paper demonstrated that CMSI tolerance to dispersion is ideal to simplify procedures employing objectives from different manufacturers in the turret. Objectives from different makes can be utilized even if they do not need to share the same thread type, as commercially available adapter rings are available that can be used to convert between several types of industry standards (SM1, RMS, M25 x 0.75 etc.). The possibility to combine objectives from different manufacturers comes at the expense of a necessary adjustment of the axial position of the sample in between turret positions, as the combined distances of the objective height and its working distance will likely not match from one objective to the next.

Modern objectives featuring extra low dispersion (ED) glass are an option to limit dispersion effects, but dispersion bias between the two arms of the interferometer and wavenumber nonlinearities in SD-OCM still justify the need for rapid, efficient dispersion compensation strategies.

The paper demonstrates the utility of CMSI in the simplification of procedures associated with the frequent change of microscope objectives in the day-to-day OCM operation. Similarly, a turret-equipped OCT microscope and conventional FFT-based OCT method may be used. Instead of memorizing masks, the correction protocol is stored and applied in synchronism with the MO change.

While the calibration of the two methods, conventional and CMSI, requires the same procedure and data, the Slave stage in CMSI and the signal processing in FFT-based OCT method differ fundamentally. Both methods deliver the strength of OCT signal via a given depth, an integral over the wavenumber range. The kernel of the integral is a product of two factors. For the FFT-based OCT method, the kernel of the integral is a product of the electrical signal corresponding to the resampled CS with a complex exponential representing a monochromatic harmonic oscillation. In CMSI, the kernel is the read CS, i.e. the data with no alteration while the exponential is represented by a complex mask, where the frequency is chirped, as explained in [21]. Both methods lead to similar results; however, the larger the bandwidth, the more demands are placed on the perfection of data resampling in the conventional FFT method. In contrast, in CMSI the demands are the same as for a narrow bandwidth. In a previous study [28], it was demonstrated that for a supercontinuum driving a spectrometer based OCT, CMSI performed slightly better in terms of axial resolution.

The acquisition of several experimental spectra is also common in the calibration phase of conventional FFT-based OCT [13], referred as PCDC method in [28]. A comparison of CMSI and FFT-based OCT in obtaining OCT cross sections can be found in [29]. The calculation of CMSI masks is only performed once and takes computationally less than a few seconds, a time that includes the saving operation as well. For the activity described in the present paper, such a calibration is required once per each microscope objective and remain stable unless hardware changes impact the spectrometer's data provision (function g) or if adjustments in fiber length or optical elements affect the dispersion balance (function h). The need for recalibration is not specific to CMSI, as FFT-based OCT methods involving resampling and linearization also require recalibration when changing the spectrometer or dispersion balance.

At the slave stage of the CMSI protocol, each mask is used to calculate the OCT signal strength from the depth at which the mask was calculated. This, in terms of time, replaces the process of correction of data for resampling in conventional FFT-based OCT. CMSI is expected to perform faster for applications requiring a low number of A-scan depth points [28], such as Gabor-based OCM, which consists in acquiring several B-scans high-NA optics at different focus positions [30]. Then from each B-scan, only a subsection of the axial range is retained, corresponding to the largest signal obtained around the focus position targeted. This operation is followed by the stitching of all subsections into a compound B-scan image. In this way, along the axial range of the compound B-scan image, all points are practically in focus. As shown in [31], CMSI has a time advantage over FFT-based processing when the number of stitched sections exceeds a few units (>4 for 512 axial points, as reported). Finally, CMSI benefited from progress in multicore Matrix computation in LabVIEW, which enabled simultaneous real-time display of multiple *en face* OCT images [32].

For high-resolution OCT using a supercontinuum source (as in this case), CMSI performed slightly better [28]. When considering applications at longer central wavelengths (e.g. 1300 or 1700 nm), broader spectral bandwidth would be required to achieve the same level of axial resolution. The main challenge would then be the assembly of a spectrometer able to detect such bandwidth. Notably, given that the current technology of InGaAs line cameras generally offers less pixels than CMOS, the increase in bandwidth could come at the cost of bandwidth per pixel, affecting the OCT axial range. In short, the difficulty would lie in the production of a densely sampled channeled spectrum spanning across a wide bandwidth, not in the application of the CMSI processing. Provided such spectrum can be captured, the steps of CMSI calibration

and mask generation would be identical. In addition to addressing the previously mentioned concern of a wider bandwidth, the application of Gabor filtering previously discussed provides compelling grounds for microscopy specialists to consider adopting CMS when utilizing a turret

In conclusion, this study aims to demonstrate the benefits of an OCM system with versatile objective change in the sample arm combined with efficient objective-specific dispersion compensation using CMSI. We believe that the proposed architecture is suited for OCM applications where multi-scale imaging is desired, or when a small feature needs to be located in a large area before high-NA imaging.

Funding. Biotechnology and Biological Sciences Research Council (BB/S0166431).

Acknowledgments. JC, MJM, AB, AP, DG and GR acknowledge the BBSRC for the research grant 5DHiResE (BB/S016643/1). MJM and AP also thank the NIHR 202879 at King's College and Moorfields Eye Hospital. DG, MJM, GS, PE and AP thank the MRC, Impact Accelerator Account, project 18557.

AB also acknowledges the support of the Royal Society, project PARSOCT, RGS/R1/221324 and the support of the Academy of Medical Sciences/the Wellcome Trust/the Government Department of Business, Energy and Industrial Strategy/the British Heart Foundation/Diabetes UK Spring-board Award SBF007\100162.

AP also acknowledges the NETLAS ITN GA GA860807, supported by the European Commission, the NIHR BRC, BRC4-05-RB413-302, Imaging, Visual Assessment & Digital Innovation, at Moorfields Eye Hospital NHS FT and UCL Institute of Ophthalmology.

Disclosures. CCR, JC, GS: Conceivable Life Sciences (London, UK) (C). AP, AB and MJM, co-inventors of patents in the name of the University of Kent.

Data availability. Data underlying the results presented in this paper are not publicly available at this time but may be obtained from the authors upon reasonable request.

References

1. S. H. Yun, G. J. Tearney, J. F. d. Boer, *et al.*, "High-speed optical frequency-domain imaging," *Opt. Express* **11**(22), 2953–2963 (2003).
2. A. G. Podoleanu, "Unique interpretation of Talbot Bands and Fourier domain white light interferometry," *Opt. Express* **15**(15), 9867–9876 (2007).
3. C. K. Hitzenberger, A. Baumgartner, W. Drexler, *et al.*, "Dispersion Effects in partial coherence interferometry: implications for intraocular ranging," *J. Biomed. Opt.* **4**(1), 144 (1999).
4. C. Chin, F. Toader, T. Feuchter, *et al.*, "Acousto-optic tunable filter for dispersion characterization of time-domain optical coherence tomography systems," *Appl. Opt.* **55**(21), 5707–5714 (2016).
5. A. Dubois, K. Grieve, G. Moneron, *et al.*, "Ultrahigh-resolution full-field optical coherence tomography," *Appl. Opt.* **43**(14), 2874–2883 (2004).
6. Z. Hu and A. M. Rollins, "Fourier domain optical coherence tomography with a linear-in-wavenumber spectrometer," *Opt. Lett.* **32**(24), 3525–3527 (2007). Publisher: Optica Publishing Group.
7. A. R. Tumlinson, B. Hofer, A. M. Winkler, *et al.*, "Inherent homogenous media dispersion compensation in frequency domain optical coherence tomography by accurate k -sampling," *Appl. Opt.* **47**(5), 687–693 (2008).
8. C. Yang and S. Yazdanfar, J. A. Izatt, "Fast-scanning dispersion-adjustable reference delay for OCT using fiber Bragg gratings," in *Optical Coherence Tomography and Coherence Techniques*, vol. 5140 (SPIE, 2003), pp. 53–59.
9. T. J. Eom, Y.-C. Ahn, C.-S. Kim, *et al.*, "Calibration and characterization protocol for spectral-domain optical coherence tomography using fiber Bragg gratings," *J. Biomed. Opt.* **16**(3), 030501 (2011).
10. T. R. Hillman and D. D. Sampson, "The effect of water dispersion and absorption on axial resolution in ultrahigh-resolution optical coherence tomography," *Opt. Express* **13**(6), 1860–1874 (2005).
11. G. J. Tearney, B. E. Bouma, and J. G. Fujimoto, "High-speed phase- and group-delay scanning with a grating-based phase control delay line," *Opt. Lett.* **22**(23), 1811–1813 (1997).
12. S. Iyer, S. Coen, and F. Vanholsbeeck, "Dual-fiber stretcher as a tunable dispersion compensator for an all-fiber optical coherence tomography system," *Opt. Lett.* **34**(19), 2903–2905 (2009).
13. Y. Yasuno, V. D. Madjarova, S. Makita, *et al.*, "Three-dimensional and high-speed swept-source optical coherence tomography for in vivo investigation of human anterior eye segments," *Opt. Express* **13**(26), 10652–10664 (2005).
14. N. Lippok, S. Coen, P. Nielsen, *et al.*, "Dispersion compensation in Fourier domain optical coherence tomography using the fractional Fourier transform," *Opt. Express* **20**(21), 23398–23413 (2012).
15. M. Wojtkowski, V. J. Srinivasan, T. H. Ko, *et al.*, "Ultrahigh-resolution, high-speed, Fourier domain optical coherence tomography and methods for dispersion compensation," *Opt. Express* **12**(11), 2404–2422 (2004).
16. G. Ni, J. Zhang, L. Liu, *et al.*, "Detection and compensation of dispersion mismatch for frequency-domain optical coherence tomography based on A-scan's spectrogram," *Opt. Express* **28**(13), 19229–19241 (2020).
17. D. Yang, W. Guo, T. Cheng, *et al.*, "Artificial neural network (ANN) for dispersion compensation of spectral domain-optical coherence tomography (SD-OCT)," *Instrumentation Science Technology* **50**(5), 560–576 (2022).

18. S. Ahmed, D. Le, T. Son, *et al.*, “ADC-Net: an open-source deep learning network for automated dispersion compensation in optical coherence tomography,” *Frontiers in Medicine* **9**, 6 (2022).
19. A. G. Podoleanu and A. Bradu, “Master–slave interferometry for parallel spectral domain interferometry sensing and versatile 3D optical coherence tomography,” *Opt. Express* **21**(16), 19324–19338 (2013).
20. A. Bradu, M. Maria, and A. G. Podoleanu, “Demonstration of tolerance to dispersion of master/slave interferometry,” *Opt. Express* **23**(11), 14148–14161 (2015).
21. S. Rivet, M. Maria, A. Bradu, *et al.*, “Complex master slave interferometry,” *Opt. Express* **24**(3), 2885–2904 (2016).
22. ‘Understanding Microscopes and Objectives | Edmund Optics,’.
23. E. Gratton and M. J. vandeVen, “Laser sources for confocal microscopy,” in *Handbook of Biological Confocal Microscopy*, Vol. 9166 (Springer US, Boston, MA, 1995), pp. 91660M–97.
24. C. Zhou, D. W. Cohen, Y. Wang, *et al.*, “Integrated optical coherence tomography and microscopy for ex vivo multiscale evaluation of human breast tissues,” *Cancer Res.* **70**(24), 10071–10079 (2010).
25. J. Xu, W. Wei, S. Song, *et al.*, “Scalable wide-field optical coherence tomography-based angiography for in vivo imaging applications,” *Biomed. Opt. Express* **7**(5), 1905–1919 (2016).
26. M. J. Marques, R. Green, R. King, *et al.*, “Sub-surface characterisation of latest-generation identification documents using optical coherence tomography,” *Science Justice* **61**(2), 119–129 (2021).
27. Y. Wei, T. Zhang, Y.-P. Wang, *et al.*, “Polar bodies in assisted reproductive technology: current progress and future perspectives,” *Biol. Reprod.* **92**(1), 1–8 (2015).
28. A. Bradu, N. M. Israelsen, M. Maria, *et al.*, “Recovering distance information in spectral domain interferometry,” *Sci. Rep.* **8**(1), 15445 (2018).
29. A. Bradu and A. G. Podoleanu, “Calibration-free B-scan images produced by master/slave optical coherence tomography,” *Opt. Lett.* **39**(3), 450–453 (2014).
30. J. P. Rolland, P. Meemon, S. Murali, *et al.*, “Gabor-based fusion technique for Optical Coherence Microscopy,” *Opt. Express* **18**(4), 3632–3642 (2010).
31. R. Cernat, A. Bradu, N. M. Israelsen, *et al.*, “Gabor fusion master slave optical coherence tomography,” *Biomed. Opt. Express* **8**(2), 813–827 (2017).
32. A. Bradu and A. G. Podoleanu, “Imaging the eye fundus with real-time en-face spectral domain optical coherence tomography,” *Biomed. Opt. Express* **5**(4), 1233–1249 (2014).